

Calibration and Registration Methods for a Condition Monitoring Multi-Sensor System

¹M. Rollett, ¹E. J. Theussl, ¹P. O’Leary, ²R. Fruhmann and ²B. Ellensohn

¹University of Leoben, Chair of Automation, Peter Tunner Strasse 25, 8700 Leoben, Austria

²eSENSEial Data Science GmbH, Roseggerstraße 12, 8700 Leoben

¹Tel.: +43 3842 402 5301, fax: +43 3842 402 5302

¹E-mail: automation@unileoben.ac.at

Received: 31 July 2020 /Accepted: 28 September 2020 /Published: 30 October 2020

Abstract: This paper presents a 10 degree-of-freedom sensor system with embedded computing power and wireless interface. The motivation is to provide a high-performance sensor system for condition monitoring, which requires minimal effort for retrofitting in existing plant and machinery. The embedded computing power enables on board calibration of the sensor module. A computational method is presented for the independent identification of the different coordinate systems, which are implicit in all real application, i.e. sensor axis to sensor housing, sensor housing to machine in manufacturing environment and the machine to the local earth coordinate system during operation in the field. The embedded computational power is used to perform geometric elliptical approximations for vibrational orbits. This eliminates the possible Gibbs error associated with elliptical Fourier descriptors. Additionally, a new statistical approach is presented for identifying periodic signals in a highly perturbed environment. Results are presented from the monitoring of large vibrating sieves; these results verify the correct functionality of the complete system and demonstrate the advantage of the new methods.

Keywords: Multi sensor system, Uncertainty analysis, Probability distribution, Condition monitoring, Retrofitting.

1. Introduction

This article is an extension to the introduced 10 degree-of-freedom (DOF) sensor system and its application in [1]. The sensor system with embedded computing power and wireless interface forms a powerful tool that fulfills the requirements for condition monitoring. The motivation is to enable simple implementation of condition monitoring in existing plant and machinery. To this end, the module combines a 10 DOF MEMS [2] sensor with an ARMv6 [3] architecture processor. This combination enables the sensor to deliver calibrated measurement results and to evaluate application specific algorithms, without the necessity for an additional computing

device. Calibrated sensors offer the advantage of interchangeability, a very important issue in industrial applications and currently uncommon with accelerometers.

Furthermore, an IEC-61131 [4] conformant power supply specification was implemented to facilitate simple integration in industrial equipment. The wireless interface supports a low effort retrofitting to existing machinery.

The primary motivation for this development is condition monitoring of orbital vibration sieves (see Fig. 1) used in material processing. However, the approaches and methods presented are applicable to a much wider range of monitoring applications. To keep the system as general as possible a MEMS device was

selected with 3-axis-accelerometer, -gyroscopes, -magnetic field sensors and a temperature sensor. Whereby, the focus on this paper is on the accelerometers, calibrated measurements and evaluation algorithms.



Fig. 1. Orbital vibration screen sieve placed in an experiment area which was monitored with the sensor module in Fig 2. Its working principal depends on the vibrational orbit it performs wrt. gravitational acceleration. Photo courtesy of IFE Aufbereitungstechnik, GmbH, Waidhofen an der Ybbs, Austria.

The efficiency of orbital sieves is dependent on the path and magnitude of oscillation and their orientation wrt. gravity. Classical accelerometers [5] measure with respect to the mounting on the machine.

Here, we present an important extension to vibration monitoring, which enables the simultaneously measurement of the oscillation wrt. multiple coordinate frames, e.g. wrt. gravity and/or the machine. The challenge here is to develop models and computation methods which enable the simultaneous identification of the respective coordinate frames from the different components of the acceleration data.

The computational power within the device has made it possible to embed geometric elliptical approximations as an alternative to elliptical Fourier descriptors [6], the new approach eliminates the difficulties associated with Gibbs error [7]; the new statistical method is presented which uses the deconvolution of the PDFs for a sine wave and a Gaussian to classify the vibrations.

Results, obtained from monitoring a large industrial orbital sieve are presented which demonstrate the correct functionality of the device and verify the proposed computational models.

2. Measurement Module

2.1. Module Specifications

The measurement module, shown in Fig. 2, integrates the MPU-9250 chip [8] together with an ARMv6 processor. The accelerometer provides a full-scale range of ± 16 g. The zero-g error is ± 60 mg for the x-axis and y-axes and ± 80 mg for the z-axis. The

zero-g change w.r.t temperature is specified as ± 1.5 mg/ $^{\circ}$ C in the temperature range of -40 $^{\circ}$ C to $+85$ $^{\circ}$ C. For further details about the specifications we refer to [8]. The embedded computer is based on an ARMV6 architecture with 1 GHz clock speed and 512 MB of memory. Power is supplied via a standard 24 V IEC61131 conformant interface. It also provides a serial communication interface for initial flashing of the boot software. The sensor system provides a wireless connection via Bluetooth or Wi-Fi, this reduces cabling effort during installation and disturbance from electromagnetic fields in an industrial environment.



Fig. 2. The 10 DOF multi-sensor system. The aluminium base plate is approximately 12 cm 4.5 cm width. It is used to flange the module to the machine.

3. Module Calibration

3.1. Calibration Model

In this article we focus on the calibration of 3-axis MEMS accelerometers. The goal of the calibration model is to correct for the rotation of the MEMS chip within the module around its origin R_m , the gains g_i and offsets c_i of the individual accelerometers axis (Fig. 4) In sum 9 parameters are to be determined which physically appear in this system. The required calibration coefficients are determined during a calibration procedure and stored in the device itself. A calibrated measurement result m_c is computed from the uncalibrated data m according to the following model:

$$m_c = GR_m m + c, \quad (1)$$

whereby R_m compensates for the rotations and results from the matrix multiplication:

$$R_m = R_z(\phi_z)R_y(\phi_y)R_x(\phi_x) = \quad (2)$$

$$= \begin{bmatrix} \cos\phi_z & -\sin\phi_z & 0 \\ \sin\phi_z & \cos\phi_z & 0 \\ 0 & 0 & 1 \end{bmatrix} \begin{bmatrix} \cos\phi_y & 0 & \sin\phi_y \\ 0 & 1 & 0 \\ -\sin\phi_y & 0 & \cos\phi_y \end{bmatrix} \begin{bmatrix} 1 & 0 & 0 \\ 0 & \cos\phi_x & -\sin\phi_x \\ 0 & \sin\phi_x & \cos\phi_x \end{bmatrix} \quad (3)$$

The order in Eq. (2) can be swapped as long it is handled consistent in further computations.

G and c are defined as:

$$\mathbf{G} = \begin{bmatrix} g_x & 0 & 0 \\ 0 & g_y & 0 \\ 0 & 0 & g_z \end{bmatrix} \quad \mathbf{c} = \begin{bmatrix} c_x \\ c_y \\ c_z \end{bmatrix} \quad (4)$$

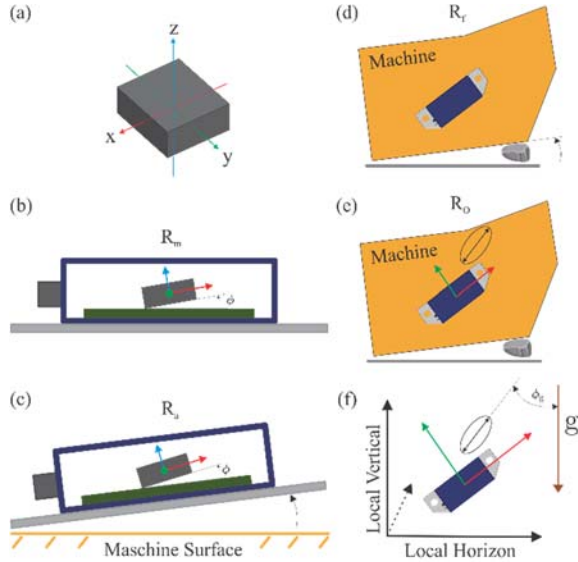


Fig. 3. The coordinate frames in the system: (a) The coordinates of the sensor module (see Fig. 4 for a more detailed drawing); (b) \mathbf{R}_m orientation of the sensor chip within the module housing, this is due to tolerances during manufacturing of the sensor module, it must be determined during calibration of the sensor; (c) A rotation \mathbf{R}_a due to tolerances in the orientation of the mounting flange on the machine, this should be determined during assembly of the machine; (d) A rotation \mathbf{R}_f emanating from the machine not being perfectly level on site. (e) Orientation \mathbf{R}_o of axes of oscillation wrt the sensor during operation. The sensor must be calibrated, and the above rotations registered, so that (f) the orientation ϕ_g of axes of oscillation wrt. the earth's gravitational field can be determined.

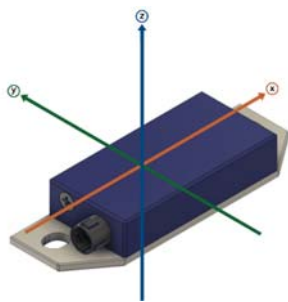


Fig. 4. Sensor module and the sensor axes orientation wrt. The module housing.

3.2. Calibration Procedure

In order to determine the calibration parameters six individual measurements in six positions were taken to measure the static acceleration of gravitation.

Therefore, a leveling table was used to orientate each sensor housing face once towards the center of gravity. This leads to the measurement of the gravitational acceleration in the positive and negative direction of each sensor axis.

A reference matrix was setup according to the performed measurements including the local gravitational acceleration which was assumed to be $g_L = 9.81 \text{ m/s}^2$:

$$\mathbf{M}_r = \begin{bmatrix} 0 & -g_L & 0 & 0 & g_L & 0 \\ g_L & 0 & 0 & -g_L & 0 & 0 \\ 0 & 0 & g_L & 0 & 0 & -g_L \end{bmatrix} \quad (5)$$

The 9 calibration parameters are determined by a variable projection where the non-linear portion R_m and the linear portion G and c from Eq. (1) are solved separately. For optimization a simplex algorithm was used to reduce the cost between the ideal measurement \mathbf{M}_r and the calibrated measurements \mathbf{M}_c computed from the optimized parameters.

$$\min \varepsilon(\boldsymbol{\phi}, \mathbf{G}, \mathbf{c}) = \min \|\mathbf{M}_r - \mathbf{M}_c\|_F \quad (6)$$

4. Reference Coordinate Frames

The goal here is to determine the respective vibration magnitudes and shape of the vibration orbit, in the application presented here it is the vibration of the sieve. To obtain these results, in a calibrated manner, it is necessary to have calibration coefficients for the sensors and to register the different coordinate frames present in the system as a whole (see Fig. 2).

4.1. Compensation for R_a

The tolerance of the mounting flange on the machine can lead to a rotation \mathbf{R}_a ; however, since the MEMS accelerometers can measure down to DC it is possible to determine \mathbf{R}_a via a static test during assembly of the machine. In the static case, the calibrated result \mathbf{m}_c should map exactly to the orientation of the earth gravitational field (measurements are in m/s^2), i.e.

$$\mathbf{m}_a = \begin{bmatrix} 9.81 \\ 0 \\ 0 \end{bmatrix} = \mathbf{R}_a \mathbf{m}_c. \quad (7)$$

4.2. Non-level Machine in the Field R_f

Similarly, the compensation of the orientation of the machine, when placed in an application, can be computed as,

$$\mathbf{m}_f = \mathbf{R}_f \mathbf{m}_a \quad (8)$$

4.3. Orientation of the Vibration Orbits

The primary axes of the vibration orbits are computed later from the oscillatory data.

5. Reference Application

The module was mounted on the orbital vibration screen sieve shown in Fig. 5. At this test the module was positioned on the inner side of the sieve. Linear, elliptical and circular vibrational orbit modes were recorded. Each measurement was observed with a sampling frequency of 2048 Hz for 1s in units of m/s^2 .

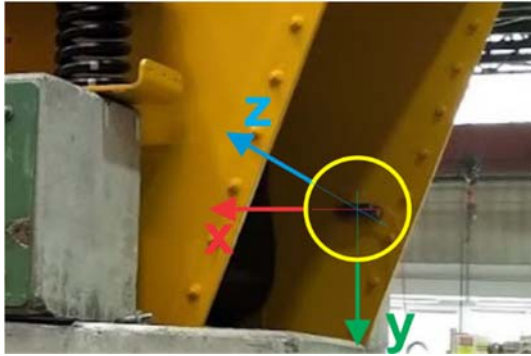


Fig. 5. Position of the sensor module on the inner side of the sieve (yellow circle) and orientation of sensor axis according to Fig. 4. In this test one axis of the sensor module was aligned close to the local horizon. Photo courtesy of IFE Aufbereitungstechnik GmbH, Waidhofen an der Ybbs, Austria.

6. Data Processing

All computations presented here start from calibrated or referenced data; for simplicity we shall denote the measurement vector here as \mathbf{m} . In the case of n measurements, they are concatenated to form the matrix \mathbf{M} , whereby the x , y and z values for the columns of \mathbf{M} . Measurements for three different oscillation modes of the sieve can be seen in Fig. 6.

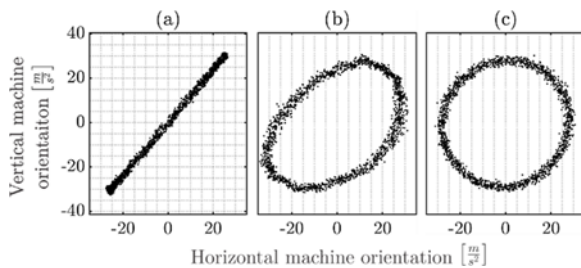


Fig. 6. Three different acceleration data sets acquired by the sensor module. A principle component analysis [8] (PCA) was performed for dimensionality reduction from 3D-axis acceleration to the main forced axes in 2D. The circular vibration screen sieve was driven in the optimal condition: (a) linear shape; in error conditions: (b) elliptical shape and (c) circular shape.

6.1. Check for Active Sensor Axes and Oscillation

The dominant direction of oscillation should be restricted to the x and y axes; the z direction should be predominantly machine noise. This is due to the manner in which the sensors are mounted on the sieve. Consequently, an initial determination which axes are active can be determined from the ratio r_R of the standard deviations σ_x , σ_y and σ_z of the accelerations, in the following manner,

$$\max \left[\frac{\sigma_x}{\sigma_z}, \frac{\sigma_y}{\sigma_z} \right] > r_R \quad (9)$$

The machine is considered to be dormant if this condition is not fulfilled.

6.2. Dominant Frequency Estimation

The dominant frequency of the oscillation is, in general, not perfectly periodic in the measurement time T ; consequently, direct Fourier methods such as the FFT will be subject to Gibbs error [9]. This error makes it difficult to estimate the parameters of a single frequency exactly and to reliably separate the DC and oscillatory components. Several efficient algorithms [10-14], primarily non-linear, have been developed to estimate the desired parameters. Here the method of variable projections is applied to the four-parameter sine wave model, defined in the IEEE standard [15]. This model can be written as a linear combination of non-linear basis functions,

$$\mathbf{y}_m = [\mathbf{1} \quad \cos(\omega t) \quad \sin(\omega t)] \begin{bmatrix} d \\ a_c \\ a_s \end{bmatrix} \quad (10)$$

Note: $\mathbf{1}$ in this equation is an $n \times 1$ vector of ones.

The method of variable projections [16, 17], is characterized by the model being a linear combination of nonlinear functions; as is our model here, see Eq. (10). Defining the basis functions:

$$\mathbf{f}_1 \triangleq \mathbf{1}, \quad (11)$$

$$\mathbf{f}_2(\omega) \triangleq \cos(\omega t) \text{ and} \quad (12)$$

$$\mathbf{f}_3(\omega) \triangleq \sin(\omega t) \quad (13)$$

and concatenating the individual basis functions into the matrix of basis functions $\mathbf{F}(\omega) = [\mathbf{f}_1, \mathbf{f}_2(\omega), \mathbf{f}_3(\omega)]$. The notation $\mathbf{F}(\omega)$ indicates that the contents of the matrix \mathbf{F} is dependent on ω . Now defining the coefficient vector $\mathbf{c} \triangleq [d, a_c, a_s]^T$ leads directly to the matrix vector equation,

$$\mathbf{y}_m = \mathbf{F}(\omega)\mathbf{c} \quad (14)$$

Given an estimate for ω a least squares estimate for \mathbf{c} is obtained from n measurements $\mathbf{y} = [y_1, \dots, y_n]^T$ by,

$$\mathbf{c} = \mathbf{F}^+(\omega)\mathbf{y}, \quad (15)$$

whereby $\mathbf{F}^+(\omega)$ denotes the pseudo-inverse of $\mathbf{F}(\omega)$; substituting Eq. (15) into (14) we obtain,

$$\mathbf{y}_m = \mathbf{F}(\omega)\mathbf{F}^+(\omega)\mathbf{y} \quad (16)$$

Note: that $\mathbf{P}(\omega) = \mathbf{F}(\omega)\mathbf{F}^+(\omega)$ is the projection onto the basis functions contained in $\mathbf{F}(\omega)$. This projection varies with ω , hence the name, method of variable projection. The residual vector is computed as $\mathbf{r} = \mathbf{y} - \mathbf{y}_m$; leading to the cost function $E(\omega)$ defined as the sum of squares of the residual r ,

$$E(\omega) = \|\mathbf{r}\|^2 \quad (17)$$

$$= \|\{\mathbf{I} - \mathbf{F}(\omega)\mathbf{F}^+(\omega)\}\mathbf{y}\|^2 \quad (18)$$

this is called the *variable projection functional* (VPF). Note that the estimation of ω is now a non-linear least squares problem in one variable. That is, the frequency can be determined without having to characterize the other sine-wave parameters.

A. Covariance propagation

If required, the method of variable projection yields a direct method of calculating the covariance for the linear coefficients. Given $\mathbf{c} = \mathbf{F}^+\mathbf{y}$, then \mathbf{L}_c the covariance of \mathbf{c} can be computed as,

$$\mathbf{L}_c = \mathbf{F}^+\mathbf{\Lambda}_y\mathbf{F}^{+T}, \quad (19)$$

whereby \mathbf{L}_c is the covariance of the stochastic portion of \mathbf{y} . If we now assume that \mathbf{y} is perturbed by iid. Gaussian noise with the standard deviation σ_y , then we obtain,

$$\mathbf{L}_c = \sigma_y^2\mathbf{F}^+\mathbf{F}^{+T} \quad (20)$$

An estimate for σ_y can be computed from the residual vector \mathbf{r} .

$$\sigma_y = \frac{1}{n-n_{df}}\|\mathbf{r}\|_2, \quad (21)$$

here n_{df} denotes the number of degrees of freedom. An example for the approximation of a noisy sine-wave is shown in Fig. 7, the corresponding covariance of the linear coefficients are given in Table 1.

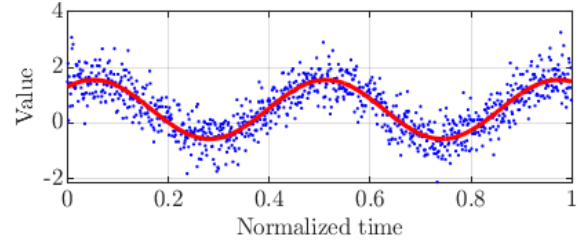


Fig. 7. Synthetic sine wave used to demonstrate the approximation and the computation of covariances. The model parameters were: $\omega = 2.2$, $d = 0.5$, $a_c = a_s = 1/\sqrt{2}$ with iid. noise with a standard deviation of $\sigma = 0.5$, $n = 1000$ samples were used. The estimation results are: $\omega = 2.1841$, $d = 0.4837$, $a_c = 0.7064$ and $a_s = 0.7058$. The corresponding covariance of the linear coefficients is shown in Table 1.

Table 1. Covariances for the test case shown in Fig. 5. The results are scaled by $1E3$ since they were very small.

Cov	d,d	d,a_c	d,a_s
d,d	0.251	-0.031	-0.020
d,a_c	-0.031	0.488	-0.028
d,a_s	-0.020	-0.028	0.513

6.3. Rotation \mathbf{R}_a : Module Housing - Machine (Assembly Registration)

To compensate mounting tolerances of the sensor module on the machine surface, the rotation \mathbf{R}_a has to be determined. A requirement for reliable result is, that the machine is perfectly levelled wrt. gravity.

A static acceleration measurement is performed to determine \mathbf{R}_a . In a static measurement only the DC-components \mathbf{M}_{DC} are measured by the accelerometers. Computing a PCA of the DC components $\mathbf{m}_{DC} = [x_{DC} \ y_{DC} \ z_{DC}]$ from the static measurement \mathbf{M}_{DC} , delivers the rotation \mathbf{M}_a as follows:

$$\mathbf{m}_{DC} = \mathbf{U}_{DC}\mathbf{S}_{DC}\mathbf{V}_{DC}^T, \quad (22)$$

where \mathbf{V}_{DC} corresponds to \mathbf{R}_a , the assembly registration. Now, the measurement rotation due to the mounting tolerances can be formulated as

$$\mathbf{M}_a = \mathbf{M}\mathbf{R}_a \quad (23)$$

The data are now exactly aligned towards the gravitational field.

6.4. Rotation \mathbf{R}_f : Machine – Field (Field-Registration)

Rough conditions in the field can make it difficult to level the machine wrt. to the gravitational field and cause a misalignment of the machine, which

is defined as a rotation \mathbf{R}_f . The rotation \mathbf{R}_f can be similar determined as \mathbf{R}_a by computing the PCA of measurements \mathbf{M}_f taken in the field of the calibrated data:

$$\mathbf{M}_f = \mathbf{U}_f \mathbf{S}_f \mathbf{V}_f^T, \quad (24)$$

where \mathbf{V}_f corresponds to \mathbf{R}_f , the field alignment registration.

6.5. The Inclination of the Machine in the Field During Operation wrt. Gravitational Field

To detect unwanted inclinations of the sieve during operation the rotation of the DC-components of the oscillating signal during operation can be monitored and compared to \mathbf{R}_f . A change in the components can indicate an unintended movement of the machine or a loosening of the measurement device.

7. Data Analysis

7.1. Determine Orbits: Dimensionality Reduction

As stated, the axes of oscillation of the sieve are restricted to either a linear or closed 2D orbit. Dimensionality reduction can be applied to the 3-axes data to determine if it is a 1D- or 2D-oscillation. A principle component analysis is applied to the calibrated measurement data:

$$\mathbf{M} = \mathbf{U} \mathbf{S} \mathbf{V}^T, \quad (25)$$

whereby the singular values s_i are contained in the diagonal of \mathbf{S} . The singular values are the two norm's of the projections of the data onto the orthogonal axes, $s_i = \sigma_i \sqrt{n}$ that is, we have a measure for the activity in each principle axes. Consequently, we can determine if it is a linear vibration or an orbital vibration. The principal components are obtained by:

$$\mathbf{P} = \mathbf{U} \mathbf{S} \quad (26)$$

whereby the principal components p_i are the single columns of \mathbf{P} .

An example of calibrated measurement data for a linear oscillation is shown in Fig. 8, two of the acceleration axes are activated, this is due to the relationship between the principle angle of oscillation and the mounting angle of the sensor. In Fig. 9 the PCA for the data presented in Fig. 8 is shown. This reveals a linear oscillation since only one axis is active in the PCA. The normalized singular values

for the presented data are: $s_1 = 1$, $s_2 = 0.0781$ and for $s_3 = 0.031$.

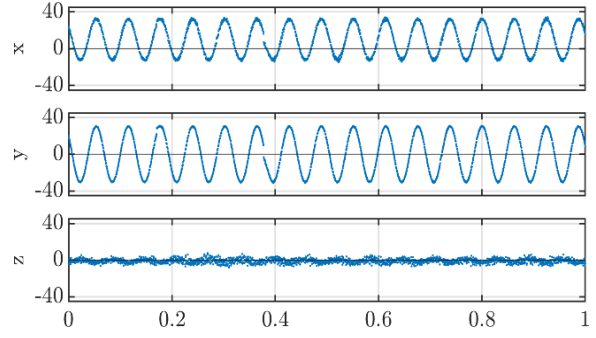


Fig. 8. This figure shows raw measurement obtained by the sensor module. An oscillation of the amplitude can be clearly seen in both axes x and y.

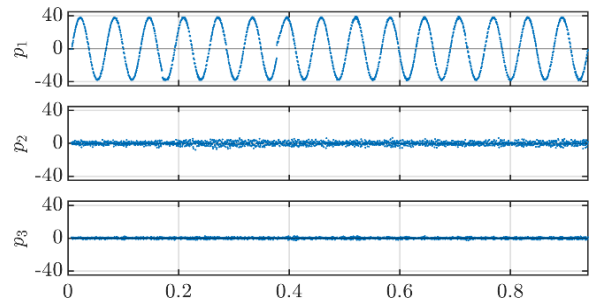


Fig. 9. The result of performing a PCA and periodicity trimming on the same data set as used in Fig. 8 reveals a linear vibration from two active sensors axes. Fig. 12(a) visualizes \mathbf{p}_1 over \mathbf{p}_2 of the same data set.

7.2. Determine Orientation \mathbf{R}_0 : Orientation of orbits wrt. Gravity

The efficiency of the sieve depends on the orientation ϕ_g of the oscillation axes wrt. the gravitational field of the earth.

In order to obtain ϕ_g the mean-free and trimmed data $\mathbf{x}_{mf} = \mathbf{x} - \bar{\mathbf{x}}$ and $\mathbf{y}_{mf} = \mathbf{y} - \bar{\mathbf{y}}$ of the measurements \mathbf{M} have to be considered in the following calculation. They are concatenated to form the matrix $\mathbf{M}_0 = [\mathbf{x}_{mf} \ \mathbf{y}_{mf}]$. A PCA is performed on \mathbf{M}_0 . The resulting components are given as follows:

$$\mathbf{M}_0 = \mathbf{U}_0 \mathbf{S}_0 \mathbf{V}_0^T \quad (27)$$

The orientation angle ϕ_g can now be extracted from the 2D rotation matrix \mathbf{V}_0 .

$$\mathbf{V}_0 = \begin{bmatrix} \cos\phi_g & -\sin\phi_g \\ \sin\phi_g & \cos\phi_g \end{bmatrix} \quad (28)$$

In order to obtain the direction ϕ_g from \mathbf{M}_0 , the four-quadrant inverse tangent is applied.

8. Orbit Analysis

To monitor the machine efficiency the orbit must be examined for their movement behavior. In this section we introduce a new statistical approach to determine vibrational orbits and compare the results with the method of elliptical Fourier descriptors (EFD).

8.1. Spectral Analysis of Vibrational Data

A spectral analysis is performed to yield the maximum frequency f_{\max} of oscillation and the respective magnitude a_{\max} of both considered principal components \mathbf{p}_1 and \mathbf{p}_2 . The spectrum $H_{p_1}(f)$ of \mathbf{p}_1 is yield by the Fourier transform \mathcal{F} of \mathbf{p}_1 :

$$H_{p_1}(f) = \mathcal{F}(\mathbf{p}_1) \quad (29)$$

whereby the maximum magnitude a_{\max,p_1} and the corresponding frequency f_{\max,p_1} is given by

$$a_{\max,p_1} = \max(H_{p_1}(f)) \quad (30)$$

The maximum magnitude and corresponding frequency of \mathbf{p}_2 can be yield in the same manner. In addition, the corresponding velocity v_{\max,p_1} and displacement s_{\max,p_1} can be computed by

$$v_{\max,p_1} = \frac{a_{\max,p_1}}{2\pi f_{\max,p_1}}, \quad (31)$$

$$s_{\max,p_1} = \frac{v_{\max,p_1}}{\pi f_{\max,p_1}} \quad (32)$$

The so obtained orbit properties of \mathbf{p}_1 and \mathbf{p}_2 can be used for approximating a geometric model to the acceleration orbit the machine runs through during operation. Fig. 14(b) presents an elliptical measurement and its approximated orbit with elliptical Fourier descriptors.

8.2. Statistical Analysis of Vibrational Data

An alternative to spectral analysis was investigated to yield a geometric approximation for the orbit. Since the acquired data of an orbit is periodic and perturbed with Gaussian noise the probability function of the principal component \mathbf{p}_1 and \mathbf{p}_2 are expected to be a composition of the probability density functions (PDF) of a sine and Gauss [9]. Fig. 10 visualizes both PDFs and their composition. The PDF of a sinusoidal is given by

$$f(x) = \frac{1}{\pi \sqrt{1 - \left(\frac{x}{R}\right)^2}}, \quad (33)$$

where x is the equally spaced distribution of the amplitude R of the sine.

The well-known PDF of a Gaussian distribution is defined as

$$g(x) = \frac{1}{\sqrt{2\pi}\sigma} \exp\left(-\frac{(x-\mu)^2}{\sigma^2}\right), \quad (34)$$

where σ is the standard deviation and μ the mean.

The expected model of the vibrational data is a mixture of both distributions. It can be formulated by the convolution of both PDFs $f(x)$ and $g(x)$, analytically by

$$P_{f(x)*g(x)} = (f * g)(x) := \int_a^b f(\tau)g(\tau - x)d\tau \quad (35)$$

In this application the convolution is done numerically based on Eq. (17) and Eq. (18).

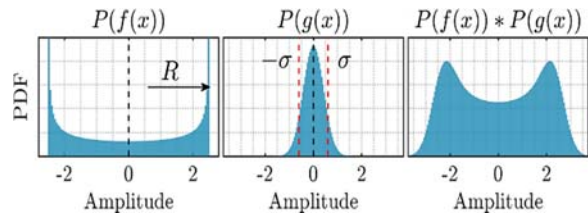


Fig. 10. Symbolic PDFs: left of a sine; middle of a Gauss; right: their convolution.

8.3. Statistical Analysis with Deconvolution of the Noise and Sinusoidal Components

A non-linear continuous approximation for the PDF $P_{f(x)*g(x)}(x)$ is performed to yield an adequate approximation of the model for the discrete PDF $P_{PC}(\hat{x})$ of the observations \hat{x} of each principal component respectively. The cost between both PDFs is therefore minimized wrt. to the parameters R , σ and μ .

$$\min \varepsilon(\sigma, R) = \min \left\| P_{f(x)*g(x)}(x) - P_{PC}(\hat{x}) \right\|_1 \quad (36)$$

8.4. Parameter Optimization

To find the parameters of the non-linear problem, a simplex algorithm for non-linear functions was used. The following iterative steps are performed for the optimization for each principal component respectively:

- 1) Compute the deconvoluted sine- and Gauss-PDF, $P(f(x))$ and $P(g(x))$ with the corresponding parameters;

- 2) Convolute both PDFs to yield the mixed distribution $P_{f(x)*g(x)}$;
- 3) Compute the 1-norm of the residual between $P_{f(x)*g(x)}$ and P_p .

The iteration is performed until certain termination criteria are fulfilled. Those criteria are e.g. when a certain number of iterations is reached or both, the function value and the parameter value change is smaller than a defined value.

9. Results

9.1. Module Calibration - Results

For the computation of the calibration parameters, 40000 samples in each sensor axis direction were recorded. The initial values for the non-linear parameter were set to $\phi_i = 0$. The linear parameter for the main axis were set to $g_i = 9.81$ and for the cross-axis $g_{i,j} = 0$. The initial offsets were set to $c_i = 0$. Table 2 shows the result of the module calibration.

Table 2. Results of the calibration parameters. All cross gains were calculated to be 0.

Axis	Gain g_i	Offset c_i	Angle ϕ_i
	[-]	[mg]	[°]
x	0.9971	26.8196	3.2975
y	0.9993	27.4924	-1.1998
z	0.9835	21.1213	0.4977

The gain g_i is shown close to be 1 in each axis. No correlated cross gains $g_{i,j}$ appeared. The offsets lie in the tolerances of $\pm 60 \text{ mg}$ for the x- and y-axis and $\pm 80 \text{ mg}$ for the z-axis, as specified in the sensor data-sheet. The assembly tolerances of the sensor chip orientation were found to be between approximately -1.2° in y and 3.3° in x.

9.2. Statistical - and Fourier - Results

The results of the statistical approach for a linear (see Fig. 11), elliptical (Fig. 12) and a circular (Fig. 13) are presented in histograms in the corresponding figures. However, each histogram shows the difference between the actual principle components $P(\hat{x})$ (red bars) and the calculated model $P(x)$ (blue bars), where $P(x)$ is the result from the non-linear approximation of the PDFs. The optimized PDFs reveal a good estimate for the amplitude R of each principal component and the sensor noise σ . The different shapes of the distributions of the histograms are clearly visible; The circular PDF in Fig. 11 shows a quite steep gradient at the sides for both principal components. The PDF of the linear data set in Fig. 9 directly reveals the characteristically histogram for a motion in p_1 . The histogram of p_2 in

Fig. 9 reveals the residual noise of the second principle component. It can be seen that the result of the model matches the data from $p_2(\hat{x})$, which follows a Gaussian distribution.

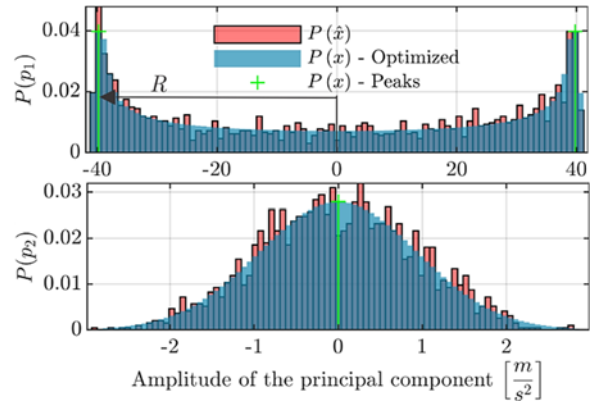


Fig. 11. Linear orbit: PDF (red) and optimized PDF (green) of the 2D principal components corresponding to the linear orbit dataset in Fig. 6(a). The optimization took place with 1-Norm residual. Note that the amplitude scale of p_2 is different to p_1 .

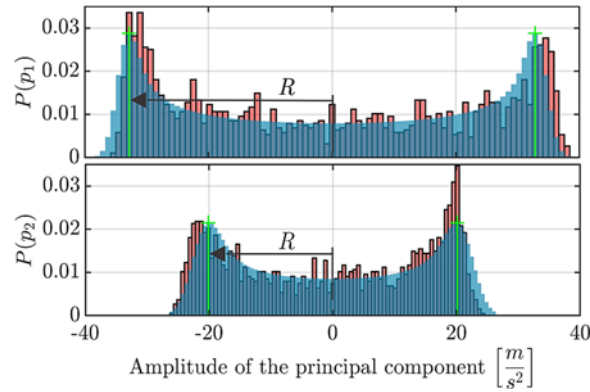


Fig. 12. Elliptical orbit: PDF (red) and optimized PDF (green) of the 2D principal components corresponding to the elliptical orbit dataset in Fig. 5(b). The optimization took place with 1-Norm residual.

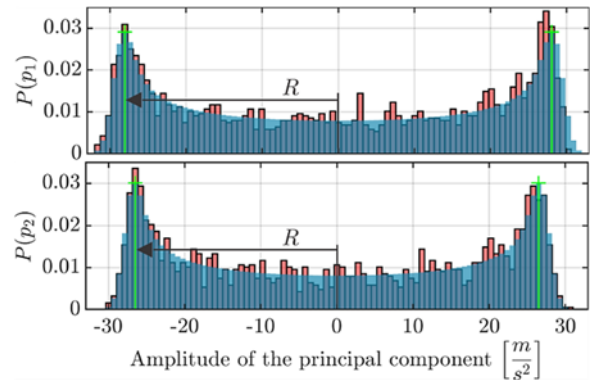


Fig. 13. Circular orbit: PDF (red) and optimized PDF (green) of the 2D principal components corresponding to the circular orbit dataset in Fig. 5(c). The optimization took place with 1-Norm residual.

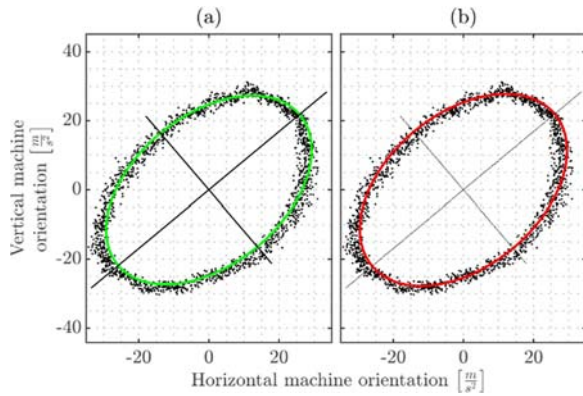


Fig. 14. (a) The orbital model yield by the ellipse computation with the optimized parameters. (b) The orbital model yield by the synthesized EFD results with $n=1$ harmonics.

Table 3 summarizes the results yield by the non-linear optimization for the amplitude R and the standard deviation σ for each principal component. It also shows the results of the orbit approximation with elliptical Fourier descriptors with $n = 1$ harmonics. The amplitudes R between the PDF and EFD results differ for the elliptical and circular measurement by approximately 5%. The difference between the amplitudes of the linear measurement differ significant for the principal component p_2 . The uncertainty in the amplitudes are clearly better for the EFD results.

Table 3. Results of the statistical characterization and of the elliptical Fourier descriptors.

Orbit	p_i	PDF Parameters		EFD Parameters	
		R	σ	R	σ
		[m/s ²]		[m/s ²]	
Linear	1	39.982	1.254	38.264	1.713
	2	0.132	1.322	1.2022	0.894
Elliptical	1	33.889	2.218	34.13	1.525
	2	21.434	3.001	21.979	1.573
Circular	1	28.977	1.633	28.775	1.284
	2	27.421	1.5	27.459	1.381

10. Conclusion

This paper introduces the combination of a MEMS-sensor together with computational power and implemented algorithms in a compact sensor module. That allows the sensor module to provide calibrated acceleration measurements and the analysis of measurements. The challenge of retrofitting machines is facilitated since the necessity of an external computation device is no longer required. The advantage of the MEMS-sensor to measure acceleration down to DC enables the identification of the orientations of the vibrational orbit axes wrt. to the gravitational field; this parameter is decisive for the

effectiveness of vibration sieves. In addition, machine alignment registration in the field can be achieved. Through comparison, it can be concluded, that the presented statistical deconvolution based method is an alternative to approximate elliptical orbits, which avoids the difficulties associated with Gibbs errors.

References

- [1]. M. Rollett, E. J. Theussl, P. O'Leary, R. Fruhmann, B. Ellensohn, A Miniature Multi-sensor System and it's Application in a Condition Monitoring, in *Proceedings of the 6th International Conference on Sensors Engineering and Electronics Instrumentation Advances (SEIA'2020)*, Porto, Portugal, 23-25 September 2020, pp. 75-81.
- [2]. K. Maenaka, MEMS Inertial Sensors and Their Application, in *Proceedings of the IEEE 5th International Conference on Networked Sensing Systems (INSS'08)*, 2008, pp. 71 - 73.
- [3]. ARM@v6-M Architecture Reference Manual, *ARM Limited or Its Affiliates*, 2017.
- [4]. K. Thramboulidis, G. Frey, An MDD process for IEC 61131-based industrial systems, *ETFA2011*, 2011.
- [5]. S. Thanagasundram, Comparison of integrated micro-electrical-mechanical system and piezoelectric accelerometers for machine condition monitoring, in *Proceedings of the Institution of Mechanical Engineers, Part C: Journal of Mechanical Engineering Science*, 2006.
- [6]. F. P. Kuhl, C. R. Giardina, Elliptical Fourier features of a closed contour, *Computer Graphics and Image Processing*, Vol. 18, Issue 3, 1982, pp. 236-258.
- [7]. A. J. Jerri, The Gibbs phenomenon in Fourier analysis, splines and wavelet approximations, *Springer Science & Business Media*, Vol. 446, 2013.
- [8]. MPU-9250 Product Specification Revision 1.1, *InvenSense Inc.*, 2016.
- [9]. P. O'Leary, M. Harker, Polynomial approximation: An alternative to windowing in Fourier analysis, in *Proceedings of the IEEE International Conference on Instrumentation and Measurement Technology*, 2011, pp. 1-6.
- [10]. M. Fonseca da Silva, P. M. Ramos, A. Serra, A new four parameter sine fitting technique, *Measurement*, Vol. 35, Issue 2, 2004, pp. 131-137, 2 Special Issues: Vibration Measurement by Laser Techniques Advances and Applications and in *Proceedings of the 7th Workshop on ADC Modelling and Testing*. [Online]. Available: <http://www.sciencedirect.com/science/article/pii/S0263224103000812>.
- [11]. K. Hejn, A. Pacut, Effective resolution of analog to digital converters, *IEEE Instrumentation Measurement Magazine*, Vol. 6, Issue 3, 2003, pp. 48-55.
- [12]. I. Kollar, J. J. Blair, Improved determination of the best fitting sine wave in ADC testing, *IEEE Transactions on Instrumentation and Measurement*, Vol. 54, Issue 5, 2005, pp. 1978-1983.
- [13]. K. Hejn, D. Morling, A semi-fixed frequency method for evaluating the effective resolution of A/D converters, in *Proceedings of the IEEE Conference on Instrumentation and Measurement Technology*, 1991, pp. 51-54.

- [14]. K. F. Chen, Estimating parameters of a sine wave by separable nonlinear least squares fitting, *IEEE Transactions on Instrumentation and Measurement*, Vol. 59, Issue 12, 2010, pp. 3214–3217.
- [15]. IEEE standard for digitizing waveform recorders, *IEEE Std. 1057-2017* (Revision of IEEE Std. 1057-2007), 2018, pp. 1–10.
- [16]. G. H. Golub, V. Pereyra, The differentiation of pseudo-inverses and nonlinear least squares problems whose variables separate, *SIAM Journal on Numerical Analysis*, Vol. 10, Issue 2, 1973, pp. 413–432.
- [17]. G. Golub, V. Pereyra, Separable nonlinear least squares: the variable projection method and its applications, *Inverse Problems*, Vol. 19, Issue 2, 2003, pp. R1–R26.



Published by International Frequency Sensor Association (IFSA) Publishing, S. L., 2020 (<http://www.sensorsportal.com>).

Easy and quick sensors systems development

- 16 measuring modes
- Frequency range from 0.05 Hz up to 7.5 MHz (120 MHz)
- Programmable accuracy from 1 % up to 0.001 %
- RS232 (USB optional)

sales@sensorsportal.com
http://www.sensorsportal.com/HTML/E-SHOP/PRODUCTS_4/Evaluation_board.htm